RESEARCH ARTICLE | AUGUST 09 2024

Effect of vibrational excitation on vorticity amplification and transportation in shock/isotropic turbulence interaction: A numerical investigation

Fangcheng Shi (施方成) ; Peixu Guo (郭培旭) ; Hongpeng Liu (刘宏鹏) ; Tiantian Wang (王田天)

Physics of Fluids 36, 085140 (2024)
https://doi.org/10.1063/5.0221514

Physics of Fluids ARTICLE pubs.aip.org/aip/pof

Effect of vibrational excitation on vorticity amplification and transportation in shock/isotropic turbulence interaction: A numerical investigation

Cite as: Phys. Fluids **36**, 085140 (2024); doi: 10.1063/5.0221514
Submitted: 1 June 2024 · Accepted: 26 July 2024 ·
Published Online: 9 August 2024

Fangcheng Shi (施方成),[1] Peixu Guo (郭培旭),[2] Hongpeng Liu (刘宏鹏),[3] and Tiantian Wang (王田天)[1,a)]

AFFILIATIONS

[1]College of Mechanical and Vehicle Engineering, Hunan University, Changsha, China
[2]Department of Aeronautical and Aviation Engineering, The Hong Kong Polytechnic University, Kowloon, Hong Kong
[3]College of Aerospace Science and Engineering, National University of Defense Technology, Changsha, China

[a)]Author to whom correspondence should be addressed: wangtt@hnu.edu.cn

ABSTRACT

The canonical shock/isotropic turbulence interaction (SITI) at high shock Mach numbers (M_s) is studied by conducting direct numerical simulation (DNS) for thermally perfect gas (TPG) and calorically perfect gas (CPG). Combining DNS with linear interaction analysis (LIA), the amplification of vorticity variance across the shock wave is studied. It is found that the changes in vortical velocity fluctuation amplitude and turbulent length scales under vibrational excitation have a competitive effect on vorticity amplification. The latter is dominant and leads to the transverse vorticity amplification increasing by 32.2% at $M_s = 6.0$. Based on the LIA theory, a vorticity amplification model for SITI considering vibrational excitation is established. Furthermore, the impact of vibrational excitation on the downstream vorticity transportation is examined through an analysis of the transport equation. The vibrational excitation strengthens both the vortex stretching and viscous dissipation of streamwise vorticity but only alters the viscous dissipation of transverse vorticity. Then, the vorticity transportations of different turbulent structures for CPG and TPG are compared. The comparison indicates that the increment of vortex stretching for streamwise vorticity variance is sustained by the enhanced turbulent structures corresponding to the stable-node/saddle/saddle, and the rapid decay of transverse vorticity variance for TPG is associated with the enhanced viscous dissipation of the nonfocal turbulent structure.

I. INTRODUCTION

The interaction of a shock wave with turbulence has received extensive attention as a fundamental problem in fluid mechanics. It affects the dynamic characteristics of the shock wave[1] and changes the turbulence intensity and turbulence scales,[2] leading to high-intensity noise,[3] force load oscillation, and high heat transfer over high-speed aerospace vehicles.[4] A deeper understanding of the shock/turbulence interaction (STI) is essential for the advancement of high-speed vehicles.

The canonical shock/isotropic turbulence interaction (SITI) is a "building block" problem of STI, and it has been investigated theoretically, experimentally, and computationally. The linear interaction analysis (LIA) was successfully used to analyze the interaction of a shock wave with the vortical wave[5]/turbulence,[6] the acoustic wave[7]/turbulence,[8] vortical–entropy turbulence,[9] and the two-dimensional spots.[10] Recently, Chen[11] extended LIA to investigate pressure-dilatation in SITI and got an analytical expression as a function of the mean Mach number. Apart from LIA, rapid distortion theory (RDT) has also been successfully applied to SITI.[12,13] It relies on more restrictive assumptions than LIA, and its application is limited. The majority of experimental studies for SITI were conducted in a shock tube with a traveling planar shock wave, while some studies were carried out in wind tunnel facilities to observe the turbulence passing through a stationary shock wave. The experimental results reported an amplification of turbulence intensity,[14] pressure fluctuation,[15] and entropic mode,[16] and a decrease in the longitudinal integral length scale[17] and Taylor microscales[18] across the shock wave. Controlling the upstream turbulence characteristics and establishing the correlation between the three Kovásznay modes in experiments is challenging. Direct numerical simulation (DNS) is another effective method to gain insight into SITI. It has been applied to qualitatively verify some theoretical and experimental results, such as the increment of turbulent kinetic energy

and the decrement of turbulent length scales across the shock wave.[19] Considering the reduction of Kolmogorov length scale across the shock wave, Larsson and Lele[20] applied a finer grid to improve the resolution of the post-shock turbulence, and they pointed out some qualitative differences with previous work.[21,22] Then, DNS was also undertaken to study the shock structure,[23] the amplification factor of velocity fluctuations,[24] and the changes in thermodynamic fluctuations[25,26] and turbulence noise.[27]

Vorticity is a key variable in turbulent flows, and the fluctuations of vorticity play an important role in turbulence dynamics. The vorticity fluctuations determine the solenoidal dissipation, which is often used to characterize the turbulent dissipation rate in the Reynolds-averaged Navier–Stokes framework.[28] By using DNS, Lee *et al.*[19] found that the transverse vorticity fluctuation was amplified across the shock wave, while the streamwise vorticity fluctuation remained relatively unchanged. Of special interest is the effect of shock strength on vorticity fluctuations in SITI. The LIA theory predicts the enhanced amplification of transverse vorticity variance as the shock Mach number increases. However, the prediction contradicts to some experimental results.[18] By analyzing the DNS data, Larsson and Lele[20] pointed out that the amplifications of streamwise and transverse vorticity variances increased as the shock Mach number rose from 1.28 to 1.87. Accordingly, the downstream turbulence indicated a local axisymmetric state with a reduced vortex-stretching mechanism. The peak of the probability density function (PDF) of transverse vorticity fluctuation decreased with the strengthening of the shock wave.[29]

In hypersonic flows, such as external flows over hypersonic vehicles, the intense shock wave leads to high temperatures and activates complex real gas effects, including vibrational excitation and chemical reactions, which would impact SITI. By assuming local thermodynamic equilibrium conditions, Samuel and Ghosh[30] performed simulations to study the effect of thermodynamic and transport properties. They discovered that the thermodynamic property has a greater influence on the downstream vorticity evolution. In addition, several theoretical studies have been conducted. Hejranfar and Rahmani[31] studied the influence of real gas effects on thermodynamic disturbances based on the one-dimensional Euler equation. The one-dimensional assumption could not account for the effects of shock deformation. Huete *et al.*[32] developed the LIA theory for thermochemical-equilibrium gas and pointed out that the amplification of enstrophy increased under the thermochemical-equilibrium effect. Since the viscous effect is ignored in theoretical analyses, the above theories can only predict turbulence characteristics in the near field downstream of a shock wave and cannot accurately describe the vorticity transportation.

The aforementioned studies have made some important achievements in the SITI problem concerning intense shock waves. However, to the authors' knowledge, the impact of vibrational excitation on vorticity amplification and transportation has not yet been investigated in detail. In this paper, fully resolved DNSs at different shock Mach numbers are carried out. Combining with the LIA theory for thermally perfect gas (TPG), the mechanisms of vorticity amplification across a shock wave and the downstream vorticity transportation are revealed.

The content of this paper is organized as follows: First of all, the adopted computational methods for DNS are described, including the governing equations, the numerical algorithm, and the simulation setup. Then, simulations for two-dimensional shock/vortical wave interaction are conducted to study the influence of vibrational excitation on velocity and vorticity fluctuations. Next, the simulation results for three-dimensional shock/vortical isotropic turbulence interaction are presented, and the impact of vibrational excitation on vorticity amplification and transportation is analyzed by combining DNS with the LIA theory. Conclusions are presented in Sec. V. Explicit LIA formulas that incorporate the effect of vibrational excitation are described in the Appendix.

II. COMPUTATIONAL METHODS

A. Governing equations and numerical algorithm

The unsteady compressible Navier–Stokes equations for TPG are solved to study the vibrational excitation effect, which can be written as the conservation form in the Cartesian coordinate system $Ox_1x_2x_3$ as follows:

$$\begin{cases} \dfrac{\partial}{\partial t}\rho + \dfrac{\partial}{\partial x_j}(\rho u_j) = 0, \\ \dfrac{\partial}{\partial t}(\rho u_i) + \dfrac{\partial}{\partial x_j}(\rho u_i u_j + \delta_{ij} p) = \dfrac{\partial}{\partial x_j}\sigma_{ij}, \\ \dfrac{\partial}{\partial t}\left(\rho e + \dfrac{1}{2}\rho u_i u_i\right) + \dfrac{\partial}{\partial x_j}\left[\left(\rho e + \dfrac{1}{2}\rho u_i u_i + p\right)u_j\right] = \dfrac{\partial}{\partial x_j}(u_i\sigma_{ij} - q_j), \end{cases} \tag{1}$$

where t and x_i represent time and spatial coordinates of the Cartesian coordinate system, respectively. The summation convention over repeated indices is applied. ρ, u_i, T, and p denote the density, velocity, temperature, and pressure, respectively. The internal energy per unit mass e, shear stress σ_{ij}, and heat flux q_j are defined as

$$\begin{cases} e = h - \dfrac{p}{\rho}, \\ \sigma_{ij} = \mu\left(\dfrac{\partial u_i}{\partial x_j} + \dfrac{\partial u_j}{\partial x_i} - \dfrac{2}{3}\dfrac{\partial u_k}{\partial x_k}\delta_{ij}\right), \\ q_j = -\kappa\dfrac{\partial T}{\partial x_j}. \end{cases} \tag{2}$$

The static enthalpy of the gas mixture consisting of ns species is related to the mass fraction and static enthalpy of the species s, Y_s and h_s, by

$$h = \sum_{s=1}^{ns} Y_s h_s, \tag{3}$$

h_s is fitted by the polynomial of gas temperature for TPG.[33] The static enthalpy for calorically perfect gas (CPG) can be obtained by $h = c_p T$, where the specific heat capacity at constant pressure c_p is a constant. The transport coefficients, including the molecular viscosity and thermal conductivity, are important for simulating the transportation processes, which are calculated based on Wilke's mixing rules,

$$\begin{cases} \mu = \displaystyle\sum_{s=1}^{ns}\left[\mu_s X_s \Big/ \left(\sum_{n=1}^{ns}\Phi_{sn}X_n\right)\right], \\ \kappa = \displaystyle\sum_{s=1}^{ns}\left[\kappa_s X_s \Big/ \left(\sum_{n=1}^{ns}\Phi_{sn}X_n\right)\right], \end{cases} \tag{4}$$

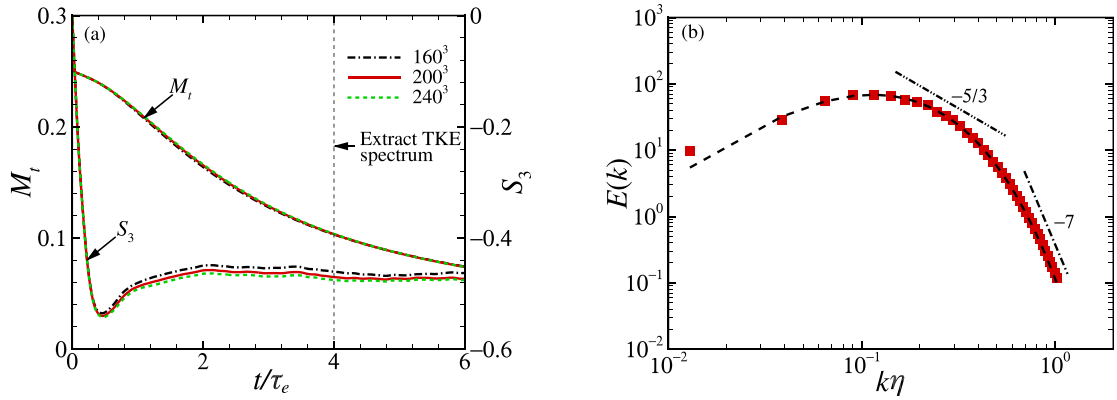

FIG. 1. (a) Time history of turbulent Mach number and velocity derivative skewness. (b) Turbulent kinetic energy spectrum at $t = 4\tau_e$, dashed line: $E_{\text{fit}}(k)$.

where X_s is the mole fraction and Φ_{sn} is the partition function of species s. The molecular viscosity and thermal conductivity for individual species, μ_s and κ_s, are calculated by Gupta's temperature fitting expressions.[34]

The state equation of TPG is given as

$$p = \rho T \mathscr{R} \sum_{s=1}^{ns} \frac{Y_s}{m_s} = \rho T R, \tag{5}$$

where $\mathscr{R}$ is the universal constant and m_s is the molecular weight of the species s. The gas adopted in this study is air and it consists of two species: N_2 and O_2.

The simulations in this paper are conducted using a high-order finite-difference in-house code that has been validated for SITI in previous studies.[27] The seventh-order WENO-Z scheme,[35] combined with the freestream preservation technique,[36] and the fourth-order central difference scheme are used for the discretization of inviscid fluxes and viscous fluxes, respectively. The time advancement is performed using a third-order Runge–Kutta method.[37] Additionally, the parallel simulation is conducted using the massage passing interface (MPI) based on the space-decomposed algorithm. The simulations are performed on a computer with 2×AMD 7713 models (512 GB memory). The case with a 1160×200^2 grid for CPG takes about 150 h. By not using the freestream preservation technique, the simulated flowfield shows a larger error, although 11% of computational time can be saved.

B. Simulation set-up

The simulation domain is a cuboid of size $(6\pi \times 2\pi \times 2\pi)$, which extends from -2π to 4π in the shock normal (streamwise) direction. Regarding the coordinate system, x_1, x_2, and x_3 are defined as the streamwise, transverse, and spanwise directions, respectively. The isotropic turbulence is convected into the domain from the left surface using Taylor's hypothesis and interacts with the shock wave at $x_1 = 0$. We use the subscripts $_{\text{u}}$ and $_{\text{d}}$ to represent upstream and downstream of the shock wave, respectively. The overline $\overline{(\cdot)}$ denotes an average over the transverse direction and over time. The upstream mean temperature $\overline{T}_{\text{u}}$ is 293.15 K. We adjust the shock Mach number, $M_s = \overline{u}_{1,\text{u}}/\sqrt{\gamma R \overline{T}_{\text{u}}} = 4.0$, 6.0, and 8.0, to change the degree of vibrational excitation.

The inflow turbulence is generated separately by the precursor DNS for decaying isotropic turbulence in a cube of length 2π. We use Rogallo's method[38] to generate the initial solenoidal velocity field with the turbulent kinetic energy (TKE) spectrum $E(k) \sim k^4 e^{-2k^2/6^2}$. The pressure and temperature fields are initialized by solving the Poisson equation.[39] The turbulent Mach number M_t and Taylor-scale Reynolds number Re_λ at the initial time are 0.25 and 70.0, respectively. The simulations are carried out using three different grids, 160^3, 200^3, and 240^3, to conduct convergence tests. Figure 1(a) shows the evolution of the turbulent Mach number M_t and velocity derivative skewness S_3, where the time is dimensionless using the initial eddy turnover time τ_e. The small difference between the results labeled with 200^3 and 240^3 verifies the grid independence. A sharp decrease in S_3 is followed by relaxation to a stable value in the interval (0.4, 0.6) after $2\tau_e$, indicating that the turbulence is well developed.[40] The turbulent fluctuations at $t = 4\tau_e$ are extracted from the flowfield and specified as the inflow turbulence for SITI, at which moment $M_t \approx 0.10$ and $Re_\lambda \approx 20.0$. The TKE spectrum $E(k)$ at $t = 4\tau_e$ is shown in Fig. 1(b). There is a straight region in the spectrum near $k\eta \approx 1$ with a slope of -7, which is consistent with Batchelor's analysis of the energy spectrum in the turbulent dissipative subregion.[41] The TKE spectrum fitting against DNS data at $4\tau_e$,

$$E_{\text{fit}}(k) = 68.58\left(\frac{k}{4.411}\right)^{2.527} e^{-3.959\left[\left(\frac{k}{4.411}\right)^{0.6383}-1\right]} \tag{6}$$

is used to perform LIA in the subsequent study.

III. INTERACTION OF A SHOCK WAVE WITH TWO-DIMENSIONAL VORTICAL WAVE

The vortical isotropic turbulence can be represented as the linear superposition of vortical Fourier modes,[6] and the three-dimensional shock/vortical isotropic turbulence interaction is related to the two-dimensional shock/vortical wave interaction. In this section, we investigate the influence of vibrational excitation on the shock/vortical wave interaction through numerical simulations in inviscid flows combining with LIA. The LIA theory for TPG is described in detail in the Appendix.

Numerical simulations are performed for $M_s = 6.0$ and $\overline{T}_{\text{u}} = 293.15$ K. The upstream velocity fluctuations associated with the inflow vortical wave are

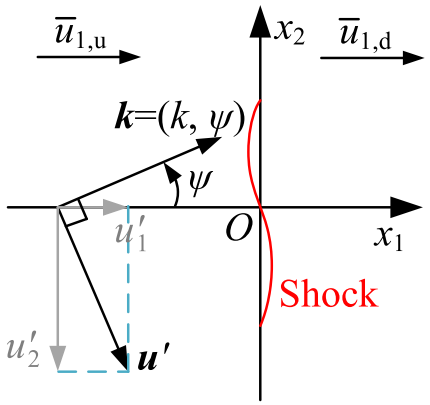

FIG. 2. Schematic of the two-dimensional shock/vortical wave interaction.

$$\begin{cases} \dfrac{u'_{1,u}}{\bar{u}_{1,u}} = Ane^{i\left[km\left(x_1-\bar{u}_{1,u}t\right)+knx_2\right]} \\ \dfrac{u'_{2,u}}{\bar{u}_{1,u}} = -Ame^{i\left[km\left(x_1-\bar{u}_{1,u}t\right)+knx_2\right]} \end{cases}, \quad m=\cos(\psi), n=\sin(\psi), \quad (7)$$

where k and ψ represent the wavenumber and incidence angle, respectively, as shown in Fig. 2. In order to avoid the nonlinear effect, the magnitude of the velocity fluctuation is taken as a small value ($A = 0.02$). The simulation domain is a rectangle of size $\left(\frac{6\pi}{km}, \frac{2\pi}{kn}\right)$, and the inflow vortical wave is convected into the domain from the left boundary and interacts with the shock wave at $x_1 = 0$. Figure 3(a) presents the instantaneous distribution of the transverse velocity fluctuation $u'_{2,u}$ at $t = 10\frac{2\pi}{km\bar{u}_{1,u}}$. It is shown that the shock wave is distorted by shock/vortical wave interaction. The shock deformation can be computed by the shock position function Eq. (A11) in LIA, which is also presented in Fig. 3(b) and compares well with the simulation result.

Then, we discuss the influence of vibrational excitation on shock deformation based on LIA. According to the shock position function Eq. (A11), the amplitude of shock deformation is determined by $|L|$. The ratio of $|L|_{TPG}$ and $|L|_{CPG}$ at different incident angles is shown in

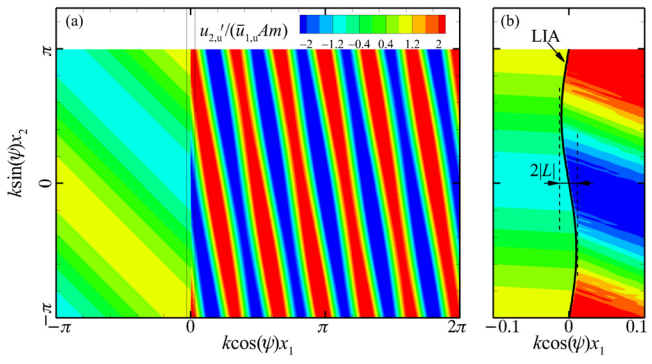

FIG. 3. (a) Contour of the transverse velocity fluctuation field at $t = 10\frac{2\pi}{km\bar{u}_{1,u}}$ for the upstream vortical wave of $(k, \psi) = (10\pi, \pi/3)$ for TPG. (b) Enlarged view of the shock location.

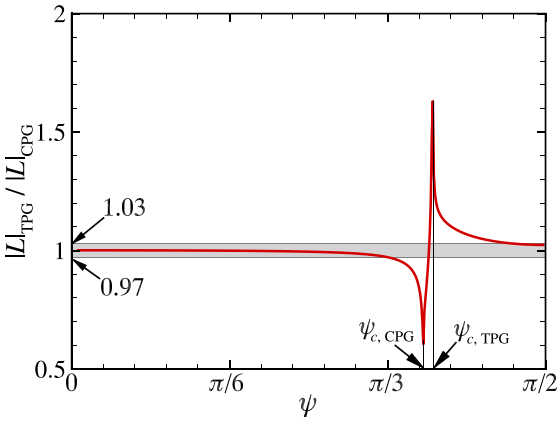

FIG. 4. Ratio of $|L|_{TPG}$ and $|L|_{CPG}$ at different incident angles. The shaded part represents $\frac{||L|_{TPG}-|L|_{CPG}|}{|L|_{CPG}} < 3\%$.

Fig. 4. When ψ equals the critical incident angle, $\psi_c = \text{acot}\left(\sqrt{(\bar{c}^2_{1,d} - \bar{u}^2_{1,d})/\bar{u}^2_{1,u}}\right)$, the amplitude of shock deformation reaches its maximum. It is found that vibrational excitation increases the critical incident angle. The influence of vibrational excitation on shock deformation mainly focuses on $\psi \approx \psi_c$. For the case where $\psi < \psi_{c,CPG}$, vibrational excitation attenuates the shock deformation; for $\psi > \psi_{c,TPG}$, it has a strengthening effect on the shock deformation.

LIA shows that the downstream velocity fluctuations consist of vortical and acoustic waves as Eq. (A9). Vortical waves incident at small ψ lead to propagating vortical and acoustic waves, while those incident at high ψ result in propagating vortical waves and evanescent acoustic waves. The shock/vortical wave interaction is then separated into a propagating regime ($\psi < \psi_c$) and an evanescent regime ($\psi > \psi_c$).[9] Figures 5(a) and 5(b) compare the downstream velocity fluctuations along the streamwise direction at $\psi = \pi/3$ and $4\pi/9$, respectively, to study the effect of vibrational excitation on $u'_{1,d}$ and $u'_{2,d}$. As $\psi = \pi/3 < \psi_c$, it is found that vibrational excitation reduces the magnitude of $u'_{1,d}$, but has little effect on the magnitude of $u'_{2,d}$. As $\psi = 4\pi/9 > \psi_c$, vibrational excitation reduces the magnitude of $u'_{1,d}$ and increases the magnitude of $u'_{2,d}$. Additionally, the wavelength of velocity fluctuation is shortened by vibrational excitation due to the reduced mean velocity.

According to Eq. (7), the spanwise component of the upstream vorticity fluctuation is given as

$$\frac{\omega'_{3,u}}{\bar{u}_{1,u}} = -iAke^{i\left[km\left(x_1-\bar{u}_{1,u}t\right)+knx_2\right]}. \quad (8)$$

Unlike the downstream velocity fluctuations that consist of vortical and acoustic modes, the spanwise component of the downstream vorticity fluctuations is dominated by the vortical mode, which can be predicted by LIA,

$$\frac{\omega'_{3,d}}{\bar{u}_{1,u}} = -iGk\left(n + \frac{m^2r^2}{n}\right)e^{i\left[km\left(rx_1-\bar{u}_{1,u}t\right)+knx_2\right]}. \quad (9)$$

Because the viscous effect and nonlinear effect are ignored in LIA, the magnitude of $\omega'_{3,d}$ is not changed along the streamwise direction.

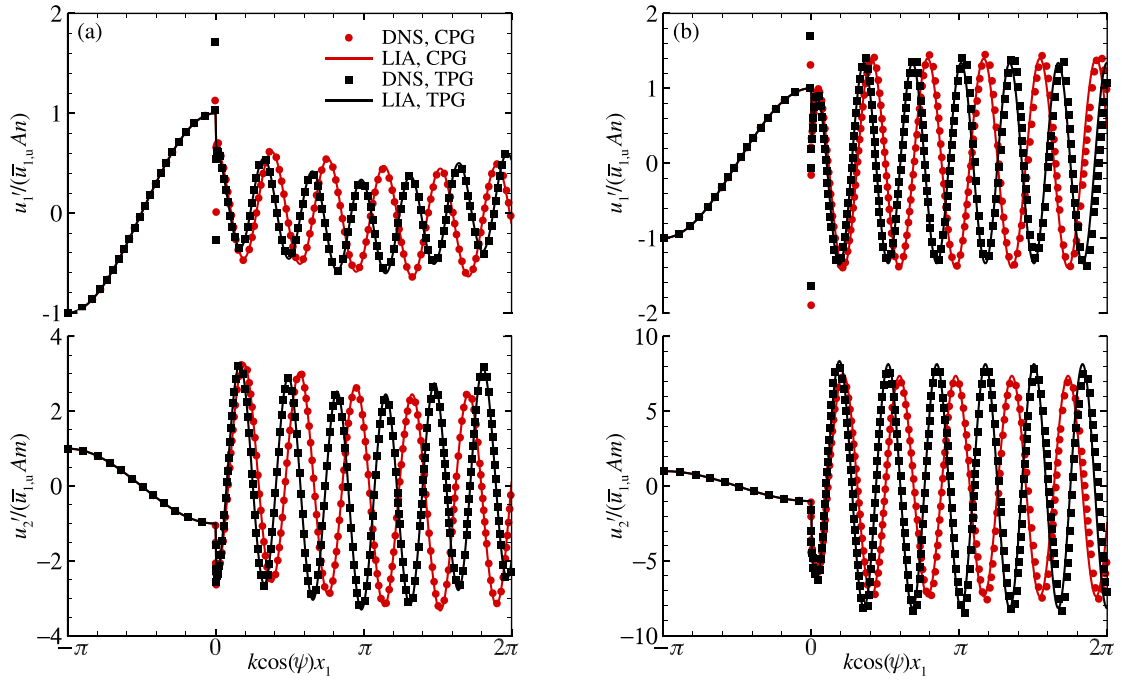

FIG. 5. Instantaneous velocity fluctuation at $x_2 = 0$. (a) $(k, \psi) = (10\pi, \pi/3)$ and (b) $(k, \psi) = (10\pi, 4\pi/9)$.

Figure 6 shows the ratio of $|\omega_{3,d}'|$ and $|\omega_{3,u}'|$ for shock/vortical wave interaction at $M_s = 6.0$. It is found that the value of $|\omega_{3,d}'|/|\omega_{3,u}'|$ is obviously increased under the vibrational excitation effect. The linearization of Euler equation yields the following equation for the vorticity fluctuation:

$$\frac{\partial \overline{u}_1 \omega_3'}{\partial x_1} = -\frac{1}{\overline{\rho}^2}\frac{\partial \rho'}{\partial x_2}\frac{\partial \overline{p}}{\partial x_1} + \frac{1}{\overline{\rho}^2}\frac{\partial p'}{\partial x_2}\frac{\partial \overline{\rho}}{\partial x_1}. \tag{10}$$

Considering the upstream vortical wave, the vorticity fluctuation across the shock wave satisfies $(\overline{u}_1\omega_3')_{x_1/L_\varepsilon=0^-} = (\overline{u}_1\omega_3')_{x_1/L_\varepsilon=0^+}$ at $\psi = 0$. Accordingly,

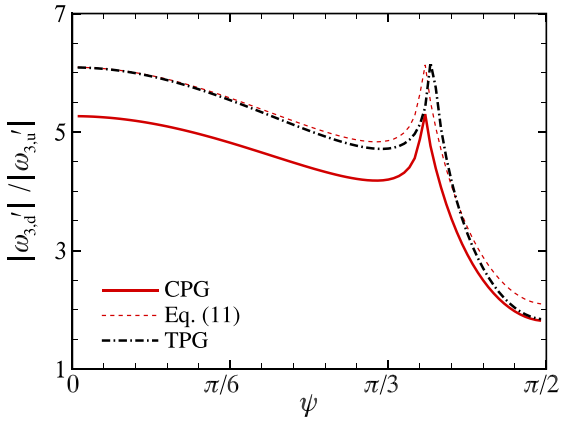

FIG. 6. Ratio of $|\omega_{3,d}'|$ and $|\omega_{3,u}'|$ at different incident angles.

$$\frac{|\omega_{3,d}'|_{TPG}}{|\omega_{3,d}'|_{CPG}} = \frac{|\omega_3'|_{x_1/L_\varepsilon=0^+,TPG}}{|\omega_3'|_{x_1/L_\varepsilon=0^+,CPG}} = \frac{(\overline{u}_{1,d})_{CPG}}{(\overline{u}_{1,d})_{TPG}}. \tag{11}$$

By using this equation, we can predict the influence of vibrational excitation on downstream vorticity fluctuation, as presented by a thin dashed line in Fig. 6. When the incidence angle is small, the increment of vorticity fluctuation caused by the vibrational excitation effect is mainly induced by the change in mean streamwise velocity.

IV. INTERACTION OF A SHOCK WAVE WITH VORTICAL ISOTROPIC TURBULENCE

A. Grid independence

The inflow turbulence is convected downstream and interacts with the shock wave at $x_1 = 0$. Figure 7 shows the computed instantaneous snapshot of eddies, which are extracted by the Q-criterion and colored by the magnitude of vorticity fluctuation $|\omega'|$. The post-shock turbulent structure is compressed and becomes anisotropic, with most eddies oriented in the tangential direction of the shock wave.[27] It has been observed that the vorticity fluctuation amplifies as turbulence passes through the shock wave and then rapidly decays in the downstream flow.

We performed grid independence tests for various computational grids. Taking the case $M_s = 6.0$ for TPG as an example, three sets of grids, 860×160^2 (grid 1), 1160×200^2 (grid 2), and 1448×240^2 (grid 3), are selected to carry out simulations. Figure 8 displays three sets of grids in the $x_1 - x_2$ plane. The distribution of spanwise grid points is the same as that applied for decaying isotropic turbulence in Sec. II B, while the streamwise grid points are clustered around the shock wave by considering that SITI would decrease turbulent length scales.[20] We nondimensionalize the streamwise grid spacing Δx_1 by the spanwise dimension of the computational domain 2π, and it is given as

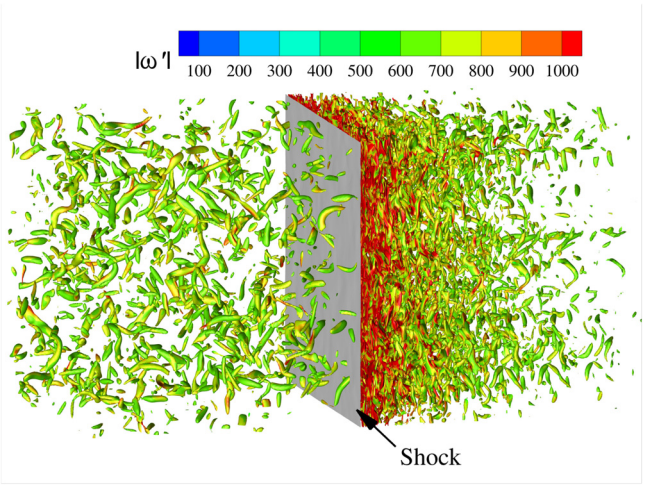

FIG. 7. Instantaneous snapshot of eddies extracted by the Q-criterion and colored by the magnitude of the vorticity fluctuation $|\omega'|$ (The shock wave is visualized by an isosurface at large density gradient).

$$\frac{\Delta x_1}{2\pi} = \left(\frac{a}{2\pi} - \frac{1}{N_2}\right)\frac{x_1}{2\pi} + \frac{a}{2\pi}, \tag{12}$$

where N_2 is the grid number in the spanwise direction and a denotes the streamwise grid spacing at $x_1 = 0$, which is 4.20×10^{-3}, 2.52×10^{-3}, and 1.79×10^{-3} for three sets of grids, respectively.

Figures 9(a) and 9(b) compare the distribution of Reynolds stresses $\overline{u_i'u_i'}$ and Kolmogorov length scale η, respectively, where the streamwise coordinate is normalized by the downstream dissipation length scale, $L_\varepsilon = [\bar{\rho}(\overline{u_i'u_i'}/2)^{1.5}/\varepsilon]_{x_1/L_\epsilon=0^+}$. The streamwise Reynolds stress $\overline{u_1'u_1'}$ at $x_1/L_\epsilon = 0^+$ is decreased by SITI, while the transverse Reynolds stress $\overline{u_2'u_2'}$ is increased. The Kolmogorov length scale at $x_1/L_\epsilon = 0^+$ is reduced by SITI. These changes are accurately captured by the LIA theory developed in the Appendix. As turbulence is convected downstream, the value of $\overline{u_1'u_1'}$ increases and then decreases, while that of $\overline{u_2'u_2'}$ decreases monotonically. Meanwhile, the Kolmogorov length scale increases gradually. The results simulated by grids 2 and 3 are basically the same, indicating that grid independence has been achieved.

B. Turbulent length scales

The Kolmogorov length scale is an important parameter characterizing the smallest turbulent structures. Based on the studies of SITI for CPG, Tian *et al.*[42] indicated that the Kolmogorov length scale would be reduced across the shock wave. Here, we first discuss the influence of vibrational excitation on the Kolmogorov length scale η. Figure 10(a) compares the value of η at $M_s = 6.0$ for CPG and TPG, indicating that vibrational excitation enhances the reduction of Kolmogorov length scale across the shock wave. The LIA-predicted difference between η_{CPG} and η_{TPG} at $x_1/L_\epsilon = 0^+$ is consistent with the simulation results. Additionally, the difference between η_{CPG} and η_{TPG} in DNS remains essentially unchanged as the turbulence is convected downstream.

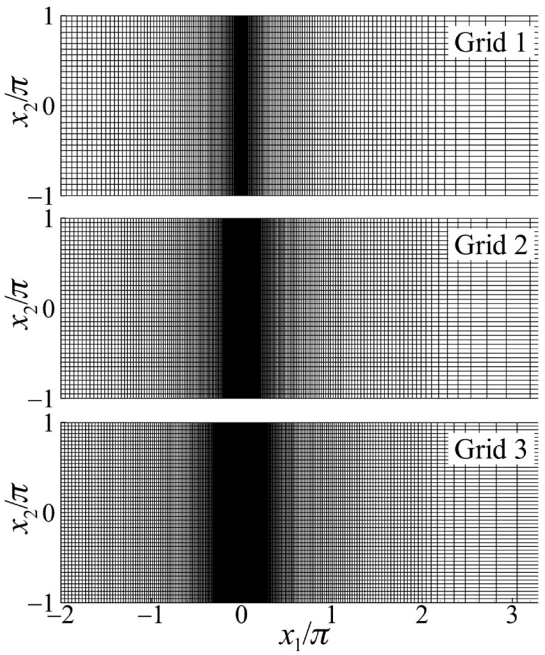

FIG. 8. Grid in the $x_1 - x_2$ plane. Every sixth grid is shown in both directions.

Furthermore, the LIA-predicted change in η across the shock wave at different shock Mach numbers is presented in Fig. 10(b). The value of $\eta_{x_1/L_\epsilon=0^+}/\eta_{x_1/L_\epsilon=0^-}$ for CPG decreases first and then increases with the increase in M_s, and its minimum value appears around $M_s \approx 3.65$. Larsson and Lele[20] stated that this is due to the density jump reaching saturation with increasing shock wave intensity and the temperature jump increasing linearly. The value of $\eta_{x_1/L_\epsilon=0^+}/\eta_{x_1/L_\epsilon=0^-}$ for TPG also exhibits a non-monotonic variation with increasing M_s, but the value of M_s at which the minimum occurs is higher ($M_s \approx 4.45$). This is a result of vibrational excitation reducing the kinematic viscosity and increasing the turbulent dissipation rate. The change in turbulent dissipation rate is related to the vorticity variance, which is explored in detail in Sec. IV C.

Then, the influence of vibrational excitation on the longitudinal Taylor microscale λ_1 is studied. The comparison of λ_1 for CPG with that for TPG at different shock Mach numbers is displayed in Fig. 11. It is found that vibrational excitation decreases the longitudinal Taylor microscale. The difference between $\lambda_{1,\mathrm{TPG}}$ and $\lambda_{1,\mathrm{CPG}}$ is first increased and then decreased as turbulence convects downstream. LIA predicts the downstream λ_1 as

$$\lambda_{1,\mathrm{d}}^2 = \frac{\int_0^{\pi/2}\int_0^{\infty}\left\{|\beta F|^2 e^{i(s-s^*)x_1} + |G|^2 + 2\mathrm{Real}\left[\beta F G^* e^{i(s^*-kmr)x_1}\right]\right\}k^2 n dk d\psi}{\int_0^{\pi/2}\int_0^{\infty}\left\{|\beta s F|^2 e^{i(s-s^*)x_1} + |kmrG|^2 + 2\mathrm{Real}\left[\beta s k m r F G^* e^{i(s^*-kmr)x_1}\right]\right\}k^2 n dk d\psi}. \tag{13}$$

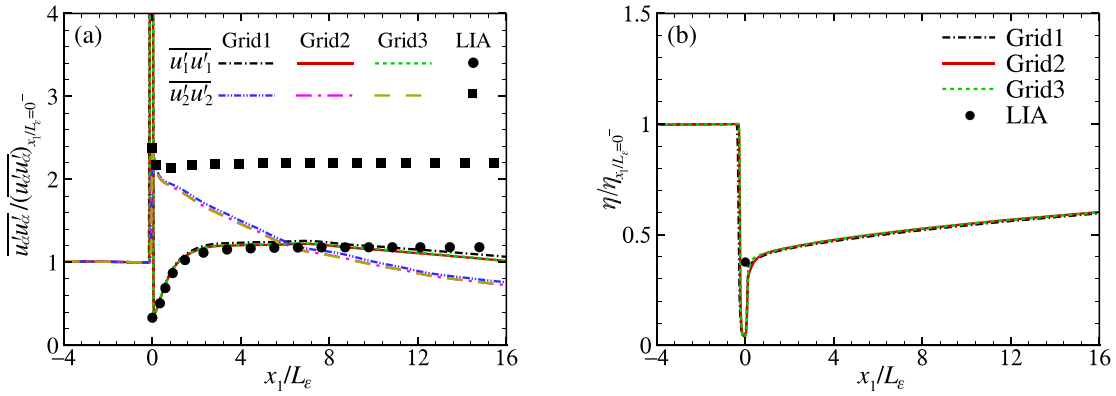

FIG. 9. Profile of turbulent statistics at $M_s = 6.0$ for TPG. (a) Reynolds stresses. (b) Kolmogorov length scale.

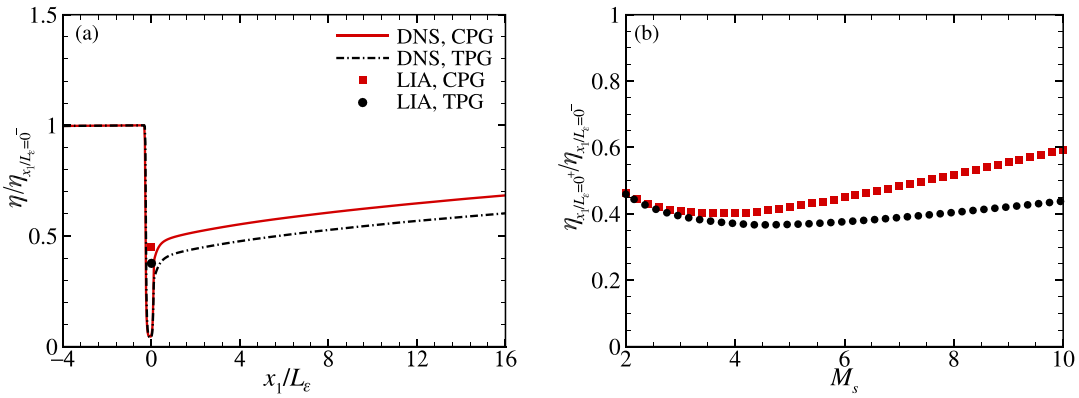

FIG. 10. (a) Evolution of Kolmogorov length scale at $M_s = 6.0$. (b) Change in η across the shock wave vs the shock Mach number, predicted by LIA.

It is indicated that the reduction of the longitudinal Taylor microscale at $x_1/L_\epsilon = 0^+$ under vibrational excitation is positively correlated with the shock wave intensity.

C. Vorticity amplification and mechanisms

For the wrinkled shock wave, SITI mainly affects the transverse vorticity variance $\overline{\omega_2'\omega_2'}$, which is amplified directly across the shock wave and then gradually decays.[20] Figure 12(a) presents the ratio of $\overline{\omega_2'\omega_2'}$ for TPG to that for CPG. It is shown that vibrational excitation increases the amplification of $\overline{\omega_2'\omega_2'}$ across the shock wave. According to Eq. (A9), LIA provides the downstream transverse vorticity variance as

$$\frac{(\overline{\omega_2'\omega_2'})_{\mathrm{d}}}{\overline{u}_{1,\mathrm{u}}^2} = \pi \int_0^{\pi}\int_0^{\infty} \left[(A_v kmr)^2 + |G|^2 \left(\frac{km^2r^2}{n} + kn \right)^2 \right] k^2 \sin(\psi) dk d\psi. \tag{14}$$

The amplification of $\overline{\omega_2'\omega_2'}$ at $x_1/L_\varepsilon = 0^+$ increases monotonically with M_s, as shown in Fig. 12(b). When the shock Mach numbers are 4.0, 6.0, and 8.0, vibrational excitation increases $\overline{\omega_2'\omega_2'}$ at $x_1/L_\varepsilon = 0^+$ by 14.8%, 32.2%, and 46.4%, respectively. These predicted values of the LIA theory agree well with the DNS results.

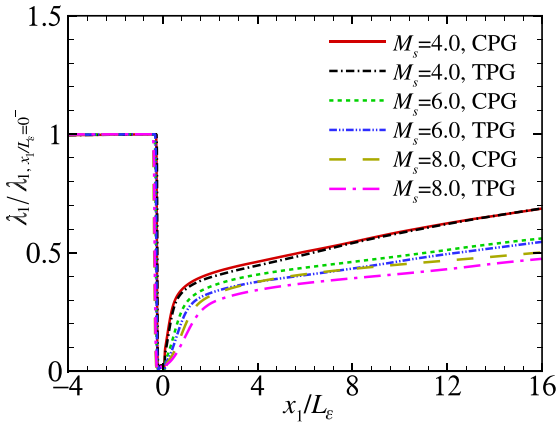

FIG. 11. Evolution of longitudinal Taylor microscale at different shock Mach numbers.

The amplitude and wavelength of the vortical velocity fluctuations are the two main factors that determine the downstream transverse vorticity variance, according to Eq. (14). Figure 13 shows the ratio of amplitude, $|G|_{\mathrm{TPG}}/|G|_{\mathrm{CPG}}$, at various M_s and ψ values,

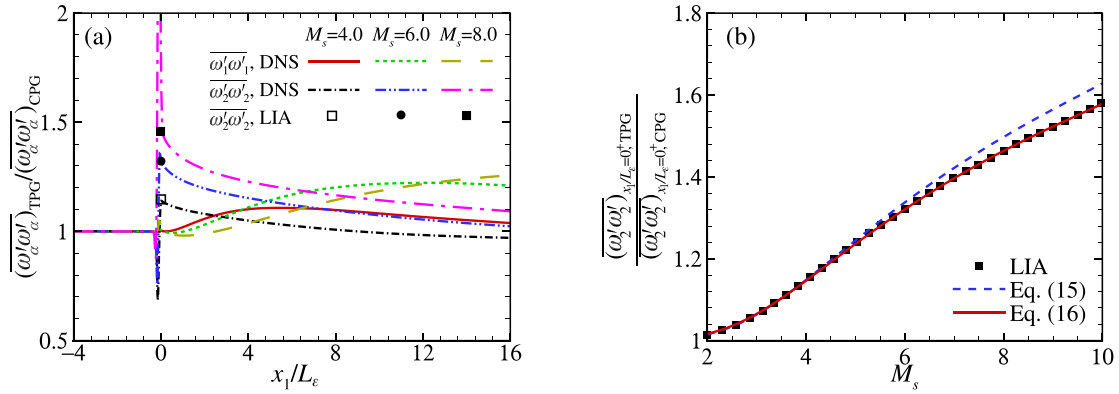

FIG. 12. (a) Ratio of vorticity variance for TPG to that for CPG with $M_s = 4.0$, 6.0, and 8.0. (b) Variation of the amplification factor as a function of M_s in LIA.

considering it is independent of wavenumbers. Vibrational excitation increases the critical angle ψ_c, resulting in the oscillation of $|G|_{TPG}/|G|_{CPG}$ in a small area around ψ_c. It is shown that the amplitude, $|G|$, is reduced by vibrational excitation. The reduction remains essentially unchanged at $\psi < \psi_{c,CPG}$, while it is enhanced and then weakened at $\psi > \psi_{c,TPG}$. Additionally, the reduction of $|G|$ is strengthened monotonically as M_s increases.

For the vortical wave with a specific value of (k, ψ), the upstream and downstream wavelengths obey the dispersion relation, and the ratio of the wavelengths is equal to $r = \overline{u}_{1,u}/\overline{u}_{1,d}$. Vibrational excitation reduces the downstream mean velocity and shortens the downstream wavelength. For three-dimensional turbulence, the streamwise Taylor microscale λ_1 and Kolmogorov length scale η are chosen to quantify the large-scale structure and the dissipation scale, respectively. As discussed in Sec. IV B, the values of both λ_1 and η are reduced by vibrational excitation. Because $(\overline{\omega_2'\omega_2'})_d$ is positively correlated with the amplitude and negatively correlated with the wavelength of vortical velocity fluctuations in Eq. (14), the changes in velocity fluctuation amplitude and turbulent length scales under vibrational excitation have a competitive effect on the vorticity amplification. The change in turbulent length scales dominates the vorticity fluctuation, resulting in a larger vorticity amplification value for TPG.

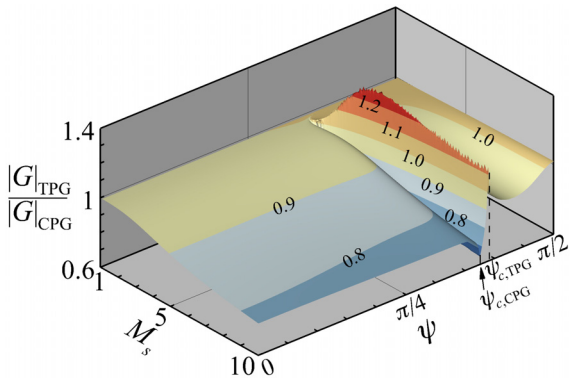

FIG. 13. Shaded surface of $|G|_{TPG}/|G|_{CPG}$ with M_s and ψ.

According to the analyses about vortical fluctuation in Sec. III, the vorticity amplification under the vibrational excitation effect can be predicted as

$$\frac{(\overline{\omega_2'\omega_2'})_{x_1/L_\varepsilon=0^+,TPG}}{(\overline{\omega_2'\omega_2'})_{x_1/L_\varepsilon=0^+,CPG}} = \frac{(\overline{\omega_3'\omega_3'})_{x_1/L_\varepsilon=0^+,TPG}}{(\overline{\omega_3'\omega_3'})_{x_1/L_\varepsilon=0^+,CPG}} \approx \left[\frac{(\overline{u}_{1,d})_{TPG}}{(\overline{u}_{1,d})_{CPG}}\right]^{-2}. \quad (15)$$

The result of this prediction model is presented in Fig. 12(b). It is found that Eq. (15) can predict the vorticity amplification at $M_s < 5.0$, but there is a significant deviation at high M_s. Since there are $\overline{T}_d$-dependent terms in the boundary conditions for TPG as shown in Eq. (A6), a temperature ratio should be introduced into the model. Then, we fix the prediction model as

$$\frac{(\overline{\omega_2'\omega_2'})_{x_1/L_\varepsilon=0^+,TPG}}{(\overline{\omega_2'\omega_2'})_{x_1/L_\varepsilon=0^+,CPG}} \approx \left[\frac{(\overline{u}_{1,d})_{TPG}}{(\overline{u}_{1,d})_{CPG}}\right]^{-3.237} \left[\frac{(\overline{T}_d)_{TPG}}{(\overline{T}_d)_{CPG}}\right]^{1.662}. \quad (16)$$

This is also shown in Fig. 12(b), which agrees well with the LIA results.

D. Vorticity transportation and turbulence structure

The amplification of $\overline{\omega_2'\omega_2'}$ behind the shock wave decays monotonically, while that of $\overline{\omega_1'\omega_1'}$ exhibits non-monotonic variation, as presented in Fig. 12(a). By taking the average over the homogeneous transverse directions and over time, the transport equation for vorticity variances suitable for SITI is written as

$$\overline{u}_1\frac{\partial\overline{\omega_\alpha'\omega_\alpha'}}{\partial x_1} = 2\overline{\omega_\alpha'\omega_j'}\overline{s}_{\alpha j} + 2\overline{\omega_\alpha'\omega_j's_{\alpha j}'} - 2\overline{\omega_\alpha'\omega_\alpha'}\overline{s}_{jj} - \overline{\omega_\alpha'\omega_\alpha's_{jj}'} - \frac{\partial}{\partial x_1}\overline{\omega_\alpha'\omega_\alpha'u_1'} + 2\varepsilon_{\alpha jk}\frac{\overline{\omega_\alpha'}\,\overline{\partial\rho}\,\overline{\partial p}}{\rho^2\,\partial x_j\,\partial x_k} + 2\varepsilon_{\alpha jk}\overline{\omega_\alpha'\frac{\partial}{\partial x_j}\left(\frac{1}{\rho}\frac{\partial\sigma_{kq}}{\partial x_q}\right)}. \quad (17)$$

The streamwise vorticity advection ($\overline{u}_1\frac{\partial\overline{\omega_1'\omega_1'}}{\partial x_1}$, term I) in the SITI problem is dominated by vortex stretching ($2\overline{\omega_1'\omega_j's_{\alpha j}'}$, term III) and viscous dissipation ($2\varepsilon_{1jk}\overline{\omega_1'\frac{\partial}{\partial x_j}\left(\frac{1}{\rho}\frac{\partial\sigma_{kq}}{\partial x_q}\right)}$, term VIII), the values of which are provided in Fig. 14(a). In the near-shock region ($0 < x_1/L_\varepsilon < 4$),

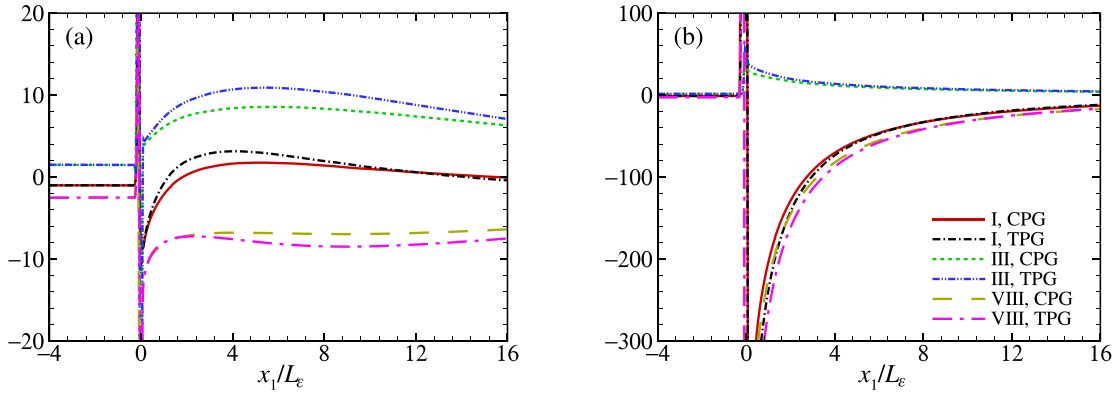

FIG. 14. Budgets of terms in the transport equation of (a) $\overline{\omega_1'\omega_1'}$ and (b) $\overline{\omega_2'\omega_2'}$. The values are normalized by the term I of (17) taken immediately upstream of the shock wave. I: vorticity advection; III: vortex stretching; and VIII: viscous dissipation.

vibrational excitation enhances the vortex-stretching effect, leading to an increase in $\overline{\omega_1'\omega_1'}$ for TPG. In the far-field region ($4 < x_1/L_\varepsilon < 8$), the viscous dissipation effect is gradually strengthened by vibrational excitation, and the difference of $\overline{\omega_1'\omega_1'}$ between CPG and TPG is reduced. As shown in Fig. 14(b), the advection of $\overline{\omega_2'\omega_2'}$ is dominated by term VIII. Vibrational excitation enhances the viscous dissipation effect in the region of $0 < x_1/L_\varepsilon < 8$, resulting in the rapid decay of $\overline{\omega_2'\omega_2'}$ for TPG.

For the purpose of identifying the vibrational excitation effect on the vorticity transportation of different turbulent structures, we first analyze the local flow pattern that is described by the second and third invariants, Q^* and R^*, of the anisotropic part of the velocity gradient tensor, $\boldsymbol{A}^* = \nabla\boldsymbol{u} - \nabla\cdot\boldsymbol{u}/3\boldsymbol{I}$, where $\boldsymbol{I}$ is the identity tensor.[43] The turbulent structures can be defined as focal ($\Delta > 0$) or nonfocal ($\Delta < 0$) depending on the discriminant, $\Delta = Q^{*3} + \frac{27}{4}R^{*2}$. The (Q^*, R^*) joint probability density functions (PDFs) at the upstream location $x_1/L_\varepsilon = -1.0$ and the downstream locations $x_1/L_\varepsilon = 0.3$, 0.6, and 4.5 are displayed in Fig. 15. For the upstream isotropic turbulence, the joint PDF has a statistical preference for the second and fourth quadrants and exhibits the well-known tear-drop shape. The shape is modified across the shock wave as the regions of unstable-focus/compressing and stable-focus/stretching are weakened and the points aligned with the left branch of $\Delta = 0$ are increased, exhibiting a "λ"-like shape at $x_1/L_\varepsilon = 0.3$. As the flow is convected downstream, the points aligned with the zero-discriminant curve are rapidly decreased and the nonfocal region ($\Delta < 0$) is gradually weakened.

The joint PDFs of two different gas models are compared to study the influence of vibrational excitation on turbulent structures. The points aligned with the zero-discriminant curve at $x_1/L_\varepsilon = 0.3$ are obviously increased under the vibrational excitation effect, especially in the region of stable-node/saddle/saddle. Additionally, the regions of unstable-focus/compression and stable-focus/stretching are weakened. These changes imply that vibrational excitation increases the turbulence structures of the nonfocal region and decreases that of the focal region. As shown in Figs. 15(c) and 15(d), the influence of vibrational excitation on the points aligned with the zero-discriminant curve is gradually diminished along the streamwise direction. The joint PDF of TPG is basically consistent with that of CPG at $x_1/L_\varepsilon = 4.5$.

Then, the contributions of different regions in the (Q^*, R^*) plane to the vorticity transportation terms are examined. The relative contribution functions of the terms III and VIII can be defined as

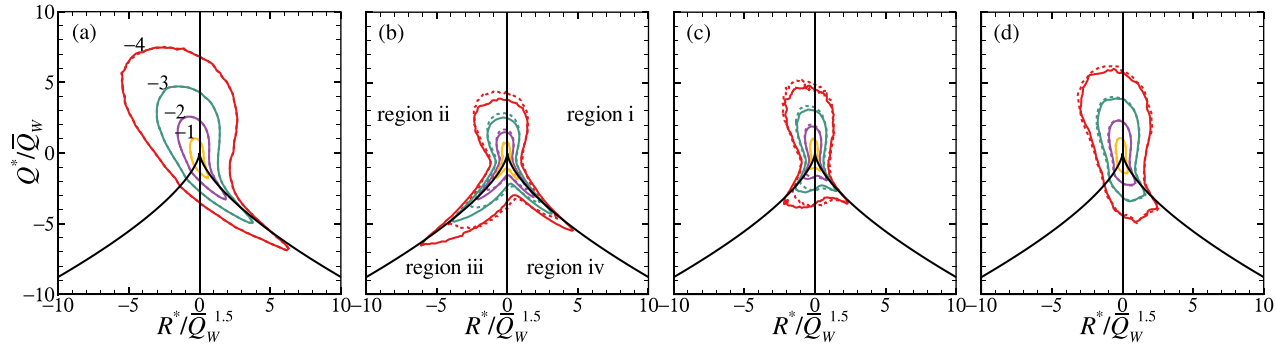

FIG. 15. Iso-contour lines of $\log_{10}\mathrm{PDF}(Q^*/Q_W, R^*/Q_W^{1.5})$ for SITI with $M_s = 6.0$ at (a) $x_1/L_\varepsilon = -1.0$, (b) $x_1/L_\varepsilon = 0.3$, (c) $x_1/L_\varepsilon = 0.6$, and (d) $x_1/L_\varepsilon = 4.5$. The axes are normalized by $\overline{Q}_W = \frac{1}{2}\overline{W_{ij}W_{ij}}$, where W_{ij} is the rotation tensor. Dashed line: CPG. Solid line: TPG. Region i: unstable-focus/compression. Region ii: stable-focus/stretching. Region iii: stable-node/saddle/saddle. Region iv: unstable-node/saddle/saddle.

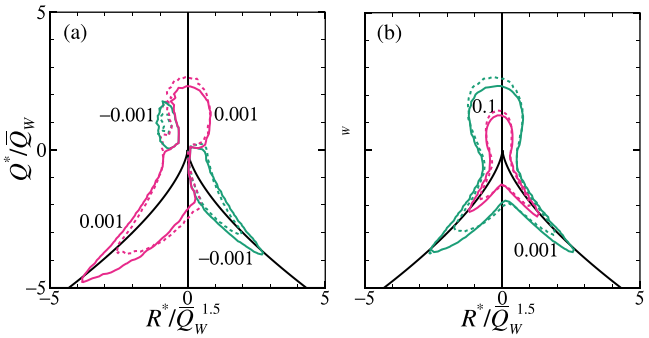

FIG. 16. Iso-contour lines of the relative contribution functions, (a) $G_{1,\mathrm{III}}$ and (b) $G_{2,\mathrm{VIII}}$, for SITI with $M_s = 6.0$. Dashed line: CPG. Solid line: TPG.

$$\begin{cases} G_{\alpha,\mathrm{III}}(Q^*,R^*) = \dfrac{g_{\alpha,\mathrm{III}}(Q^*,R^*)\cdot \mathrm{PDF}(Q^*,R^*)}{\int_{-\infty}^{\infty}\int_{-\infty}^{\infty} g_{\alpha,\mathrm{III}}(Q^*,R^*)\cdot \mathrm{PDF}(Q^*,R^*)dQ^*dR^*}, \\ G_{\alpha,\mathrm{VIII}}(Q^*,R^*) = \dfrac{g_{\alpha,\mathrm{VIII}}(Q^*,R^*)\cdot \mathrm{PDF}(Q^*,R^*)}{\int_{-\infty}^{\infty}\int_{-\infty}^{\infty} g_{\alpha,\mathrm{VIII}}(Q^*,R^*)\cdot \mathrm{PDF}(Q^*,R^*)dQ^*dR^*}, \end{cases} \tag{18}$$

where $g_{\alpha,\mathrm{III}}(Q^*,R^*)$ and $g_{\alpha,\mathrm{VIII}}(Q^*,R^*)$ are the averages of terms III and VIII on (Q^*,R^*), respectively. The turbulence in the near-field region ($x_1/L_\varepsilon = 0.3$) is studied, and we focus on $G_{1,\mathrm{III}}$ and $G_{2,\mathrm{VIII}}$ for the dominant mechanisms of vorticity transportation, as illustrated in Fig. 14. Figure 16(a) presents the contour lines of $G_{1,\mathrm{III}}$ for CPG and TPG. The contour lines of $G_{1,\mathrm{III}}$ for isotropic turbulence exhibit a butterfly-like shape with a long tail around the right branch of $\Delta = 0$, which is consistent with the result of Ref. 44. The shape of $G_{1,\mathrm{III}}$ is significantly modified by SITI, and there is a long tail around the left branch of $\Delta = 0$. Vibrational excitation enhances the vortex stretching by the turbulent structure of stable-focus/stretching, stable-node/saddle/saddle, and unstable-node/saddle/saddle, and meanwhile weakens the vortex stretching by the turbulent structure of unstable-focus/compressing. This observation reveals that the enhanced turbulent structures corresponding to the stable-node/saddle/saddle make substantial contributions to the increment of term III in Fig. 14.

The contour lines of $G_{2,\mathrm{VIII}}$ for CPG and TPG are shown in Fig. 16(b). The shape of $G_{2,\mathrm{VIII}}$ is similar to the "λ"-like shape of the PDF. The viscous dissipation of turbulent structures in the regions of stable-node/saddle/saddle and unstable-node/saddle/saddle is enhanced by vibrational excitation. This enhancement highlights the significant contributions of nonfocal turbulent structures to the increase in term VIII in Fig. 14.

V. CONCLUSION

In this paper, a series of DNSs for the shock/isotropic turbulence interaction under intense shock waves ($M_s = 4.0$, 6.0, and 8.0) are performed to investigate the effect of vibration excitation on vorticity amplification and transportation. The grid convergence test is conducted to establish the numerical accuracy of the simulated data and validate the LIA theory for TPG developed in this paper.

The shock/vortical wave interaction is first studied as one of the element problems that form the basis of the shock/isotropic turbulence interaction. It is found that the spanwise vorticity fluctuation is obviously increased by the vibrational excitation effect. This change in spanwise vorticity fluctuation is studied by comparing the velocity fluctuations for CPG with those for TPG, indicating that vibrational excitation reduces the magnitude of $u'_{1,\mathrm{d}}$, and increases the magnitude of $u'_{2,\mathrm{d}}$ when $\psi > \psi_c$ at $M_s = 6.0$. Additionally, the wavelength of the downstream velocity fluctuation is shortened by vibrational excitation.

The fully resolved DNS results for three-dimensional shock/vortical isotropic turbulence interaction are then analyzed. Combining the simulated data with the LIA theory, the mechanisms of vorticity amplification under vibrational excitation have been revealed. Vibrational excitation reduces the vortical velocity fluctuation amplitude and decreases the turbulent length scales. The latter dominates the transverse vorticity change across the shock wave and increases the vorticity amplification. Based on the LIA theory for TPG, we developed a new model to predict the vorticity amplification under the vibrational excitation effect.

Finally, the vorticity transportations for CPG and TPG are compared, and the contributions of different turbulence structures are elucidated. In the flow downstream of the shock, vibrational excitation strengthens both the vortex stretching and viscous dissipation of streamwise vorticity, but only alters the viscous dissipation of transverse vorticity, resulting in the different evolutions of $\overline{\omega'_1\omega'_1}$ and $\overline{\omega'_2\omega'_2}$. It has been found that the enhanced turbulent structures corresponding to the stable-node/saddle/saddle play an important role in increasing vortex stretching for $\overline{\omega'_1\omega'_1}$ under the effect of vibrational excitation. The decay of $\overline{\omega'_2\omega'_2}$ for TPG is mainly strengthened by the enhanced viscous dissipation due to the nonfocal turbulent structure.

In summary, the vorticity amplification and transportation are significantly altered by vibrational excitation. This work forms the foundation for developing turbulence models for SITI under vibrational excitation. The turbulent Mach number studied in this paper is low ($M_t \approx 0.10$). As the turbulent Mach number increases, the nonlinear effect in SITI is enhanced, and the application of LIA would be limited. The effect of vibration excitation on the interaction of intense shock waves and strong turbulence needs to be further investigated.

ACKNOWLEDGMENTS

This research was supported by the National Natural Science Foundation of China through Grant Nos. 12202142, 52322215, and 12102469, the Fundamental Research Funds for the Central Universities through Grant No. 531118010787, and the Key Laboratory of Hypersonic Aerodynamic Force and Heat Technology/AVIC Aerodynamics Research Institute Foundation.

AUTHOR DECLARATIONS

Conflict of Interest

The authors have no conflicts to disclose.

Author Contributions

Fangcheng Shi: Conceptualization (lead); Data curation (lead); Formal analysis (lead); Funding acquisition (equal); Investigation (lead); Methodology (lead); Software (lead); Validation (lead); Writing – original draft (lead); Writing – review & editing (equal). **Peixu Guo:** Writing – review & editing (equal). **Hongpeng Liu:** Writing – review & editing (equal). **Tian-Tian Wang:** Funding acquisition (equal).

DATA AVAILABILITY

The data that support the findings of this study are available from the corresponding author upon reasonable request.

APPENDIX: LINEAR INTERACTION ANALYSIS WITH VIBRATIONAL EXCITATION

LIA is a reliable prediction method for SITI with a large ratio of the Kolmogorov length scale to the numerical shock thickness. In this Appendix, we present the LIA theory considering the influence of vibrational excitation on SITI.

1. Rankine–Hugoniot equations for thermally perfect gas

In the Cartesian coordinate system $Ox_1x_2x_3$, the conservation equations of mass, momentum, and energy across the normal shock wave for TPG are

$$\begin{cases} \rho_u u_{1,u} = \rho_d u_{1,d}, \\ p_u + \rho_u u_{1,u}^2 = p_d + \rho_d u_{1,d}^2, \\ h_u + u_{1,u}^2/2 = h_d + u_{1,d}^2/2. \end{cases} \tag{A1}$$

The static enthalpy h is fitted by the polynomial of the gas temperature T.[33] An equivalent specific heat ratio for TPG is defined as $\Gamma = h/(h - RT)$. The equivalent Mach number is the ratio of the velocity to the equivalent sound velocity, $\mathscr{M} = u_1/\sqrt{\Gamma RT}$. Substituting these definitions into the conservation equations (A1), the density jump across the shock, ρ_d/ρ_u, can be expressed by Γ_u, Γ_d, and $\mathscr{M}_u$ as

$$\frac{\rho_d}{\rho_u} = \frac{(\Gamma_d+1)\mathscr{M}_u^2}{\frac{\Gamma_d}{\Gamma_u}(1+\Gamma_u\mathscr{M}_u^2) - \sqrt{B}}, \tag{A2a}$$

$$B = \left(\frac{\Gamma_d}{\Gamma_u}\right)^2 + \frac{2\mathscr{M}_u^2}{\Gamma_u - 1}\left[1 - \left(\frac{\Gamma_d}{\Gamma_u}\right)^2 \Gamma_u\right] + \mathscr{M}_u^4. \tag{A2b}$$

Once the density jump is obtained, the velocity jump and the pressure jump can be calculated from the conservation equations of mass and momentum,

$$\frac{u_{1,d}}{u_{1,u}} = \frac{\frac{\Gamma_d}{\Gamma_u}(1+\Gamma_u\mathscr{M}_u^2) - \sqrt{B}}{(\Gamma_d+1)\mathscr{M}_u^2}, \tag{A3a}$$

$$\frac{p_d}{p_u} = \frac{\Gamma_u\left(\mathscr{M}_u^2 + \sqrt{B}\right) + 1}{\Gamma_d + 1}. \tag{A3b}$$

The classical Rankine–Hugoniot equations for calorically perfect gas (CPG) can be obtained from Eqs. (A2) and (A3) by setting Γ equal to the constant specific heat ratio, γ.

2. Boundary conditions for fluctuations

Based on the assumption of small-amplitude fluctuations, a linear framework is used for developing the boundary conditions. The interaction between disturbances and a shock wave leads to the deformation and unsteady motion of the shock wave, as shown in Fig. 17. Assuming that $f_s(x_2, t)$ is the instantaneous shock position at $x_1 = 0$, the upstream and downstream velocity fluctuations induced by the unsteady motion of the shock wave are

$$\begin{cases} u'_{1,u} = -\partial f_s/\partial t \\ u'_{2,u} = 0 \end{cases}, \quad \begin{cases} u'_{1,d} = -\partial f_s/\partial t \\ u'_{2,d} = 0 \end{cases}. \tag{A4}$$

When the deformation angle, $\theta = \frac{\partial f_s}{\partial x_2} = O(\varepsilon)$, is small, the downstream velocity fluctuations induced by the shock deformation are

$$\begin{cases} u'_{1,d} = O(\varepsilon^2) \\ u'_{2,d} = \dfrac{\mathscr{M}_u^2 - \Gamma_d/\Gamma_u + \sqrt{B}}{(\Gamma_d+1)\mathscr{M}_u^2}\overline{u}_{1,u}\theta \end{cases}. \tag{A5}$$

Combined with the above-mentioned relations, the linearization of Rankine–Hugoniot equations (A2) and (A3) yields the following boundary conditions for two-dimensional turbulent disturbances immediately behind the shock wave:

$$\begin{aligned} &\frac{u'_{1,d} - \dfrac{\partial f_s}{\partial t}}{\overline{u}_{1,u}} + \frac{T'_d}{\overline{T}_d}\cdot\frac{\Gamma_{d,T_d}\overline{T}_d}{(\Gamma_d+1)\mathscr{M}_u^2} \\ &\quad\times\left[-\frac{1/\Gamma_u + \mathscr{M}_u^2 + \sqrt{B}}{\Gamma_d+1} + \frac{\Gamma_d/\Gamma_u}{\sqrt{B}}\left(\frac{1}{\Gamma_u} - \frac{2\mathscr{M}_u^2}{\Gamma_u - 1}\right)\right] \\ &= \frac{u'_{1,u} - \dfrac{\partial f_s}{\partial t}}{\overline{u}_{1,u}}\cdot\frac{1}{(\Gamma_d+1)\mathscr{M}_u^2}\left[\frac{\Gamma_d}{\Gamma_u}(\Gamma_u\mathscr{M}_u^2 - 1) + \frac{(\Gamma_d/\Gamma_u)^2 - \mathscr{M}_u^4}{\sqrt{B}}\right], \end{aligned} \tag{A6a}$$

$$\frac{u'_{2,d}}{\overline{u}_{1,u}} = \frac{u'_{2,u}}{\overline{u}_{1,u}} + \frac{\mathscr{M}_u^2 - \frac{\Gamma_d}{\Gamma_u} + \sqrt{B}}{(\Gamma_d+1)\mathscr{M}_u^2}\cdot\frac{\partial f_s}{\partial y}, \tag{A6b}$$

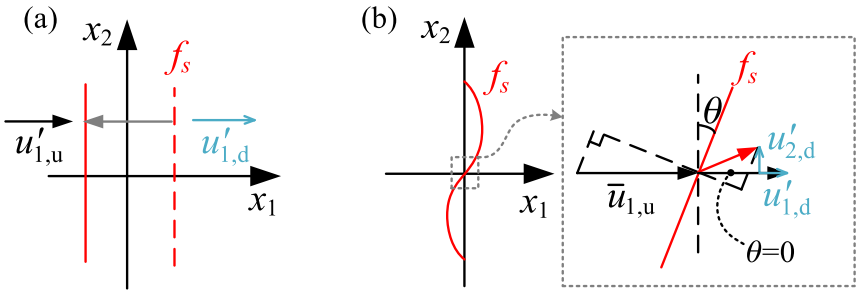

FIG. 17. Schematic of the velocity fluctuations induced by (a) unsteady motion of the shock wave and (b) shock deformation.

$$\frac{\rho'_{\mathrm{d}}}{\overline{\rho}_{\mathrm{d}}}+\frac{T'_{\mathrm{d}}}{\overline{T}_{\mathrm{d}}}\cdot\Gamma_{\mathrm{d},T_{\mathrm{d}}}\overline{T}_{\mathrm{d}} \times\frac{\left(1+\Gamma_{\mathrm{u}}\mathscr{M}_{\mathrm{u}}^2\right)\sqrt{B}+\frac{\Gamma_{\mathrm{d}}}{\Gamma_{\mathrm{u}}}\left(\frac{2\Gamma_{\mathrm{u}}}{\Gamma_{\mathrm{u}}-1}\mathscr{M}_{\mathrm{u}}^2-1\right)(\Gamma_{\mathrm{d}}+1)+\Gamma_{\mathrm{u}}B}{\Gamma_{\mathrm{u}}(\Gamma_{\mathrm{d}}+1)\cdot\left[\frac{\Gamma_{\mathrm{d}}}{\Gamma_{\mathrm{u}}}\left(1+\Gamma_{\mathrm{u}}\mathscr{M}_{\mathrm{u}}^2\right)\sqrt{B}-B\right]} =\frac{u'_{1,\mathrm{u}}}{\overline{u}_{1,\mathrm{u}}}\cdot\frac{2\frac{\Gamma_{\mathrm{d}}}{\Gamma_{\mathrm{u}}}\sqrt{B}-B+\mathscr{M}_{\mathrm{u}}^4-\left(\frac{\Gamma_{\mathrm{d}}}{\Gamma_{\mathrm{u}}}\right)^2}{\frac{\Gamma_{\mathrm{d}}}{\Gamma_{\mathrm{u}}}\left(1+\Gamma_{\mathrm{u}}\mathscr{M}_{\mathrm{u}}^2\right)\sqrt{B}-B}, \tag{A6c}$$

$$\frac{p'_{\mathrm{d}}}{\overline{p}_{\mathrm{d}}}+\frac{T'_{\mathrm{d}}}{\overline{T}_{\mathrm{d}}}\cdot\Gamma_{\mathrm{d},T_{\mathrm{d}}}\overline{T}_{\mathrm{d}}\left\{\frac{1}{\Gamma_{\mathrm{d}}+1}+\frac{2\frac{\Gamma_{\mathrm{d}}}{\Gamma_{\mathrm{u}}-1}\mathscr{M}_{\mathrm{u}}^2-\frac{\Gamma_{\mathrm{d}}}{\Gamma_{\mathrm{u}}}}{\sqrt{B}\left[\Gamma_{\mathrm{u}}\left(\mathscr{M}_{\mathrm{u}}^2+\sqrt{B}\right)+1\right]}\right\} =\frac{u'_{1,\mathrm{u}}}{\overline{u}_{1,\mathrm{u}}}\cdot\frac{2\Gamma_{\mathrm{u}}\mathscr{M}_{\mathrm{u}}^2}{\sqrt{B}\left[\Gamma_{\mathrm{u}}\left(\mathscr{M}_{\mathrm{u}}^2+\sqrt{B}\right)+1\right]}\left[\sqrt{B}+\mathscr{M}_{\mathrm{u}}^2+\frac{1-(\Gamma_{\mathrm{d}}/\Gamma_{\mathrm{u}})^2\Gamma_{\mathrm{u}}}{\Gamma_{\mathrm{u}}-1}\right], \tag{A6d}$$

where $\Gamma_{\mathrm{d},T_{\mathrm{d}}}$ is the partial derivative of Γ_{d} with respect to the temperature T_{d},

$$\Gamma_{\mathrm{d},T_{\mathrm{d}}}=\frac{R\left(\overline{h}_{\mathrm{d}}-c_{p,\mathrm{d}}\overline{T}_{\mathrm{d}}\right)}{\left(\overline{h}_{\mathrm{d}}-R\overline{T}_{\mathrm{d}}\right)^2}. \tag{A7}$$

The variable $\Gamma_{\mathrm{d},T_{\mathrm{d}}}$ is constantly equal to 0 for CPG. In this paper, we apply LIA to study the interaction of intense shock wave and vortical isotropic turbulence. The terms related to upstream temperature and pressure fluctuations in Eq. (A6) are therefore ignored.

3. Solution of the downstream turbulent fluctuations

The upstream vortical isotropic turbulence can be represented as the linear superposition of vortical Fourier modes. The wavenumber vector, $\boldsymbol{k}$, and the fluctuating velocity vector, $\boldsymbol{u}'$, of vorticity modes satisfy $\boldsymbol{k}\cdot\boldsymbol{u}'=0$. By using the cylindrical coordinate system $Ox_{1'}x_{2'}\varphi$, the three-dimensional SITI problem is related to the above-mentioned two-dimensional boundary conditions. Figure 18 displays the Cartesian coordinates and the cylindrical coordinates

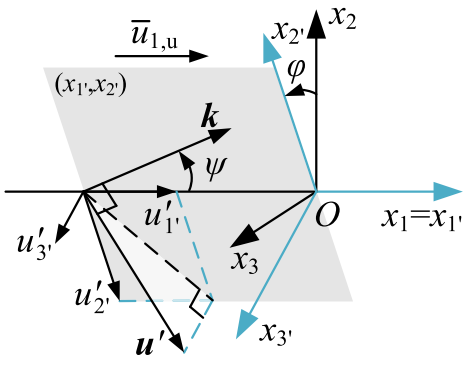

FIG. 18. Schematic of the two coordinate systems used in LIA.

associated with a wavenumber vector, $\boldsymbol{k}$, in the $(x_{1'},x_{2'})$ plane. The upstream velocity fluctuation, $\boldsymbol{u}'_{\mathrm{u}}$, is decomposed into three parts as follows:

$$\begin{cases}\dfrac{u'_{1',\mathrm{u}}}{\overline{u}_{1,\mathrm{u}}}=A_v n e^{\mathrm{i}\left[km\left(x_{1'}-\overline{u}_{1,\mathrm{u}}t\right)+knx_{2'}\right]},\\ \dfrac{u'_{2',\mathrm{u}}}{\overline{u}_{1,\mathrm{u}}}=-A_v m e^{\mathrm{i}\left[km\left(x_{1'}-\overline{u}_{1,\mathrm{u}}t\right)+knx_{2'}\right]},\ m=\cos(\psi),n=\sin(\psi).\\ \dfrac{u'_{3',\mathrm{u}}}{\overline{u}_{1,\mathrm{u}}}=A_v e^{\mathrm{i}\left[km\left(x_{1'}-\overline{u}_{1,\mathrm{u}}t\right)+knx_{2'}\right]}.\end{cases} \tag{A8}$$

The interaction between the shock wave and the vortical mode would generate entropy and acoustic modes. Therefore, expressions for the velocity and thermodynamic fluctuation fields behind the shock wave are

$$\begin{cases}\dfrac{u'_{1',\mathrm{d}}}{\overline{u}_{1,\mathrm{u}}}=\beta F e^{\mathrm{i}sx_{1'}}e^{\mathrm{i}\left(-km\overline{u}_{1,\mathrm{u}}t+knx_{2'}\right)}+Ge^{\mathrm{i}kmrx_{1'}}e^{\mathrm{i}\left(-km\overline{u}_{1,\mathrm{u}}t+knx_{2'}\right)},\\ \dfrac{u'_{2',\mathrm{d}}}{\overline{u}_{1,\mathrm{u}}}=\dfrac{kn\beta F}{s}e^{\mathrm{i}sx_{1'}}e^{\mathrm{i}\left(-km\overline{u}_{1,\mathrm{u}}t+knx_{2'}\right)}-\dfrac{mrG}{n}e^{\mathrm{i}kmrx_{1'}}e^{\mathrm{i}\left(-km\overline{u}_{1,\mathrm{u}}t+knx_{2'}\right)},\\ \dfrac{u'_{3',\mathrm{d}}}{\overline{u}_{1,\mathrm{u}}}=A_v e^{\mathrm{i}kmrx_{1'}}e^{\mathrm{i}\left(-km\overline{u}_{1,\mathrm{u}}t+knx_{2'}\right)},\\ \dfrac{\rho'_{\mathrm{d}}}{\overline{\rho}_{\mathrm{d}}}=\dfrac{1}{\gamma_{\mathrm{d}}}Fe^{\mathrm{i}sx_{1'}}e^{\mathrm{i}\left(-km\overline{u}_{1,\mathrm{u}}t+knx_{2'}\right)}+Qe^{\mathrm{i}kmrx_{1'}}e^{\mathrm{i}\left(-km\overline{u}_{1,\mathrm{u}}t+knx_{2'}\right)},\\ \dfrac{T'_{\mathrm{d}}}{\overline{T}_{\mathrm{d}}}=\dfrac{\gamma_{\mathrm{d}}-1}{\gamma_{\mathrm{d}}}Fe^{\mathrm{i}sx_{1'}}e^{\mathrm{i}\left(-km\overline{u}_{1,\mathrm{u}}t+knx_{2'}\right)}-Qe^{\mathrm{i}kmrx_{1'}}e^{\mathrm{i}\left(-km\overline{u}_{1,\mathrm{u}}t+knx_{2'}\right)},\\ \dfrac{p'_{\mathrm{d}}}{\overline{p}_{\mathrm{d}}}=Fe^{\mathrm{i}sx_{1'}}e^{\mathrm{i}\left(-km\overline{u}_{1,\mathrm{u}}t+knx_{2'}\right)},\end{cases} \tag{A9}$$

where

$$\begin{cases}s=\dfrac{-km\overline{u}_{1,\mathrm{u}}\overline{u}_{1,\mathrm{d}}+k\overline{c}_{\mathrm{d}}\sqrt{m^2\overline{u}_{1,\mathrm{u}}^2-n^2\left(\overline{c}_{\mathrm{d}}^2-\overline{u}_{1,\mathrm{d}}^2\right)}}{\overline{c}_{\mathrm{d}}^2-\overline{u}_{1,\mathrm{d}}^2},\\ \beta=\dfrac{s(kmr-s)}{s^2+(kn)^2}\dfrac{1}{\gamma_{\mathrm{d}}r}.\end{cases} \tag{A10}$$

The amplitude constants F, G, and Q are associated with the acoustic, vortical, and entropy modes, respectively. By inserting the above-mentioned expressions, (A8) and (A9), and the shock position function,

$$f_s=Le^{\mathrm{i}\left(-km\overline{u}_{1,\mathrm{u}}t+knx_{2'}\right)} \tag{A11}$$

into the boundary conditions (A6), we can get a set of linear algebraic equations. Solving these equations yields the amplitude constants, and then we can obtain the solution of SITI with vibrational excitation.

REFERENCES

[1]N. T. Clemens and V. Narayanaswamy, "Low-frequency unsteadiness of shock wave/turbulent boundary layer interactions," Annu. Rev. Fluid Mech. **46**, 469–492 (2014).

[2]M. Yu, S. Dong, P. Liu, Z. Tang, X. Yuan, and C. Xu, "Post-shock turbulence recovery in oblique-shock/turbulent boundary layer interaction flows," J. Fluid Mech. **961**, A26 (2023).
[3]F. Shi, Z. Gao, C. Jiang, and C.-H. Lee, "Numerical investigation of shock-turbulent mixing layer interaction and shock-associated noise," Phys. Fluids **33**, 025105 (2021).
[4]C. J. Roy and F. G. Blottner, "Review and assessment of turbulence models for hypersonic flows," Prog. Aerosp. Sci. **42**, 469–530 (2006).
[5]H. S. Ribner, "Convection of a pattern of vorticity through a shock wave," Report No. NACA TR-1164, 1954.
[6]H. S. Ribner, "Shock-turbulence interaction and the generation of noise," Report No. NACA TN-3255, 1954.
[7]F. K. Moore, "Unsteady oblique interaction of a shock wave with a plane disturbance," Report No. NACA TR-1165, 1954.
[8]K. Mahesh, S. Lee, S. K. Lele, and P. Moin, "The interaction of an isotropic field of acoustic waves with a shock wave," J. Fluid Mech. **300**, 383–407 (1995).
[9]K. Mahesh, S. K. Lele, and P. Moin, "The influence of entropy fluctuations on the interaction of turbulence with a shock wave," J. Fluid Mech. **334**, 353–379 (1997).
[10]G. Farag, P. Boivin, and P. Sagaut, "Interaction of two-dimensional spots with a heat releasing/absorbing shock wave: Linear interaction approximation results," J. Fluid Mech. **871**, 865–895 (2019).
[11]C. H. Chen, "Linear analysis on pressure-dilatation behind shock waves," Phys. Fluids **35**, 021701 (2023).
[12]S. K. Lele, "Shock-jump relations in a turbulent flow," Phys. Fluids A **4**, 2900–2905 (1992).
[13]T. Kitamura, K. Nagata, Y. Sakai, A. Sasoh, and Y. Ito, "Rapid distortion theory analysis on the interaction between homogeneous turbulence and a planar shock wave," J. Fluid Mech. **802**, 108–146 (2016).
[14]J. F. Debieve and J. P. Lacharme, "A shock-wave/free turbulence interaction," in *Turbulent Shear-Layer/Shock-Wave Interactions*, edited by J. Délery (Springer, Berlin, Heidelberg, 1986), pp. 393–403.
[15]S. Xanthos, G. Briassulis, and Y. Andreopoulos, "Interaction of decaying free-stream turbulence with a moving shock wave: Pressure field," J. Propul. Power **18**, 1289–1297 (2002).
[16]B. McManamen, D. Donzis, S. North, and R. Bowersox, "Velocity and temperature fluctuations in a high-speed shock-turbulence interaction," J. Fluid Mech. **913**, A10 (2021).
[17]S. Barre, D. Alem, and J. P. Bonnet, "Experimental study of a normal shock/homogeneous turbulence interaction," AIAA J. **34**, 968–974 (1996).
[18]J. H. Agui, G. Briassulis, and Y. Andreopoulos, "Studies of interactions of a propagating shock wave with decaying grid turbulence: Velocity and vorticity fields," J. Fluid Mech. **524**, 143–195 (2005).
[19]S. Lee, S. K. Lele, and P. Moin, "Direct numerical simulation of isotropic turbulence interacting with a weak shock wave," J. Fluid Mech. **251**, 533–562 (1993).
[20]J. Larsson and S. K. Lele, "Direct numerical simulation of canonical shock/turbulence interaction," Phys. Fluids **21**, 126101 (2009).
[21]S. Lee, S. K. Lele, and P. Moin, "Interaction of isotropic turbulence with shock waves: Effect of shock strength," J. Fluid Mech. **340**, 225–247 (1997).
[22]S. Jamme, J.-B. Cazalbou, F. Torres, and P. Chassaing, "Direct numerical simulation of the interaction between a shock wave and various types of isotropic turbulence," Flow, Turbul. Combust. **68**, 227–268 (2002).
[23]D. A. Donzis, "Shock structure in shock-turbulence interactions," Phys. Fluids **24**, 126101 (2012).
[24]C. H. Chen and D. A. Donzis, "Shock-turbulence interactions at high turbulence intensities," J. Fluid Mech. **870**, 813–847 (2019).
[25]N. E. Grube and M. P. Martín, "Compressibility effects on Reynolds stress amplification and shock structure in shock-isotropic turbulence interactions," J. Fluid Mech. **958**, A1 (2023).
[26]Y. P. M. Sethuraman, K. Sinha, and J. Larsson, "Thermodynamic fluctuations in canonical shock-turbulence interaction: Effect of shock strength," Theor. Comput. Fluid Dyn. **32**, 629–654 (2018).
[27]F. Shi, Z. Gao, C. Jiang, and C.-H. Lee, "Investigation on noise from shock/isotropic turbulence interaction using direct numerical simulation," J. Sound Vib. **488**, 115633 (2020).
[28]K. Sinha, "Evolution of enstrophy in shock/homogeneous turbulence interaction," J. Fluid Mech. **707**, 74–110 (2012).
[29]D. Livescu and J. Ryu, "Vorticity dynamics after the shock-turbulence interaction," Shock Waves **26**, 241–251 (2015).
[30]J. B. Samuel and S. Ghosh, "High temperature effects on DNS of shock/turbulence interaction," AIAA Paper No. 2016-3644, 2016.
[31]K. Hejranfar and S. Rahmani, "An assessment of shock-disturbances interaction considering real gas effects," J. Fluids Eng. **141**, 011201 (2018).
[32]C. Huete, A. Cuadra, M. Vera, and J. Urzay, "Thermochemical effects on hypersonic shock waves interacting with weak turbulence," Phys. Fluids **33**, 086111 (2021).
[33]M. Capitelli, G. Colonna, D. Giordano, L. Marraffa, A. Casavola, P. Minelli, D. Pagano, L. D. Pietanza, and F. Taccogna, "Tables of internal partition functions and thermodynamic properties of high-temperature Mars-atmosphere species from 50K to 50000K," ESA Scientific Technical Report No. 246, 2005.
[34]R. N. Gupta, J. M. Yos, R. A. Thompson, and K. P. Lee, "A review of reaction rates and thermodynamic and transport properties for an 11-species air model for chemical and thermal nonequilibrium calculations to 30000 K," Report No. NASA-RP-1232 (National Aeronautics and Space Administration, 1990).
[35]R. Borges, M. Carmona, B. Costa, and W. S. Don, "An improved weighted essentially non-oscillatory scheme for hyperbolic conservation laws," J. Comput. Phys. **227**, 3191–3211 (2008).
[36]T. Nonomura, D. Terakado, Y. Abe, and K. Fujii, "A new technique for free-stream preservation of finite-difference WENO on curvilinear grid," Comput. Fluids **107**, 242–255 (2015).
[37]C.-W. Shu and S. Osher, "Efficient implementation of essentially non-oscillatory shock-capturing schemes," J. Comput. Phys. **77**, 439–471 (1988).
[38]R. Rogallo, "Numerical experiments in homogeneous turbulence," Report No. NASA TM-81315, 1981.
[39]R. Samtaney, D. I. Pullin, and B. Kosović, "Direct numerical simulation of decaying compressible turbulence and shocklet statistics," Phys. Fluids **13**, 1415–1430 (2001).
[40]S. Tavoularis, J. C. Bennett, and S. Corrsin, "Velocity-derivative skewness in small Reynolds number, nearly isotropic turbulence," J. Fluid Mech. **88**, 63 (1978).
[41]G. K. Batchelor, *The Theory of Homogeneous Turbulence* (Cambridge University Press, 1959).
[42]Y. Tian, F. A. Jaberi, Z. Li, and D. Livescu, "Numerical study of variable density turbulence interaction with a normal shock wave," J. Fluid Mech. **829**, 551–588 (2017).
[43]S. Pirozzoli and F. Grasso, "Direct numerical simulations of isotropic compressible turbulence: Influence of compressibility on dynamics and structures," Phys. Fluids **16**, 4386–4407 (2004).
[44]J. Wang, Y. Shi, L.-P. Wang, Z. Xiao, X. T. He, and S. Chen, "Effect of compressibility on the small-scale structures in isotropic turbulence," J. Fluid Mech. **713**, 588–631 (2012).